Supply-Modulated Radar Transmitters With Amplitude-Modulated Pulses

Andrew Zai, *Member, IEEE*, Mauricio Pinto, *Student Member, IEEE*, Mike Coffey, *Student Member, IEEE*, and Zoya Popović, *Fellow, IEEE*

Abstract—This paper introduces an efficient radar transmitter with improved spectral confinement, enabled by a pulse waveform that contains both amplitude and frequency modulation. The theoretical behavior of the Class-B power amplifier (PA) under a Gaussian envelope is compared to that of a Class-A PA. Experimental validation is performed on a 4-W 10-GHz GaN monolithic microwave integrated circuit PA, biased in Class B with a power-added efficiency (PAE) of 50%. When driven with a Gaussian-like pulse envelope with a 5-MHz linear frequency modulation (LFM), the PA demonstrates a 31% average efficiency over the pulse duration. To improve the efficiency, a simple resonant supply modulator with a peak efficiency of 92% is used for the pulse Gaussian amplitude modulation, supplemented by pre-distortion on the PA input, while the LFM is provided through the PA input. This case results in a five-point improvement in system efficiency with an average $\text{PAE} = 40\%$ over the pulse duration for the PA alone, and with simultaneous 40-dB reduction in spectral emissions relative to a rectangular pulse with the same energy.

Index Terms—Author, please supply index terms/keywords for your paper. To download the IEEE Taxonomy go to http://www.ieee.org/documents/taxonomy_v101.pdf.

I. INTRODUCTION

MOST PULSED radar systems operate with constant amplitude pulses, where the power amplifier (PA) is biased in Class C to optimize efficiency [1]. However, the use of a Class-C PA limits the pulsed waveform to rectangular shapes because of the high nonlinearities inherent to this mode of operation, resulting in poor spectral characteristics due to fast rise and fall times of the PA. Radar spectral emissions are regulated by the National Telecommunications and Information Administration (NTIA) in the Radar Spectrum Engineering Criteria (RSEC) [2]. Emissions are regulated by a mask similar to what is shown in Fig. 1. The in-band and out-of-band emissions depend on radar characteristics such as pulse width and time-bandwidth product. The taper describing the out-of-band emissions is defined by a specific function with −40- and −60-dB levels at the edges of the band. The exact limits and widths of the regions are different for different classes of radar, but the spurious region
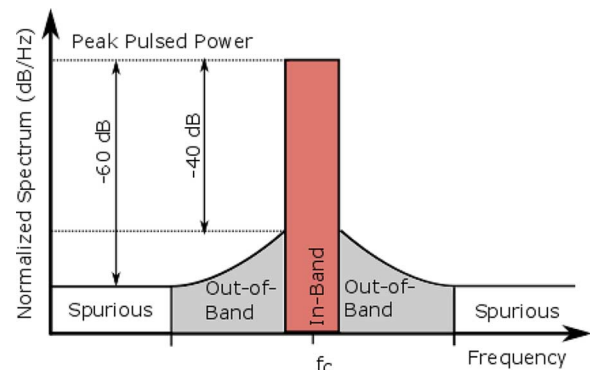
Fig. 1. Demonstration of RSEC for pulsed radar. The in-band and out-of-band bandwidths depend on characteristics such as pulse width and time-bandwidth product. The regulation on spurious emissions is −60 dB relative to peak power for this figure, but they can be as severe as −80 dB.

can have limits as strict as 80 dB below peak power. Various techniques have been used to improve the spectral confinement of pulsed radars, such as slowing down the rise and fall times at the cost of PA efficiency [1], or filtering at the expense of additional insertion loss in the high power filters.

The need for more bandwidth of wireless systems is beginning to impose more stringent requirements on radar emissions [3], [4]. Radars that operate in an increasingly congested spectral environment need to start behaving more like communications transmitters. Recently, there has been increased activity in improving the spectral properties of radars while maintaining the efficiency, e.g., optimizing the load of the PA for maximum efficiency compliant with a given adjacent channel power ratio (ACPR) [4], or applying weighting functions at the waveform generation level [5]. Envelope amplitude modulation was experimentally investigated in [5] and [6] in an out-phasing PA with up to 3-dB peak-to-average ratio waveforms and no system efficiency reported.

This paper demonstrates another method for efficient spectrally compliant radar transmitters, illustrated in Fig. 2. An efficient PA at the carrier frequency (10 GHz in this work) is driven by a frequency-modulated (FM) signal (5-MHz bandwidth in this work). The output stage supply voltage of the PA is amplitude modulated, resulting in an approximately Gaussian shaped chirped pulse at the output of the PA. A digital block at the input generates the switching times for the supply modulator, as well as the pulsed baseband signal. The pulse is rectangular and shaped by the modulated drain voltage, as with a direct polar modulator [7], [8], but pre-distortion of the pulse is required for
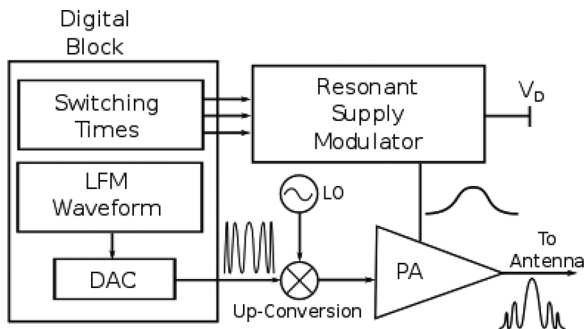
Fig. 2. Block diagram of a radar transmitter with the pulse envelope modulated by a resonant supply modulator.
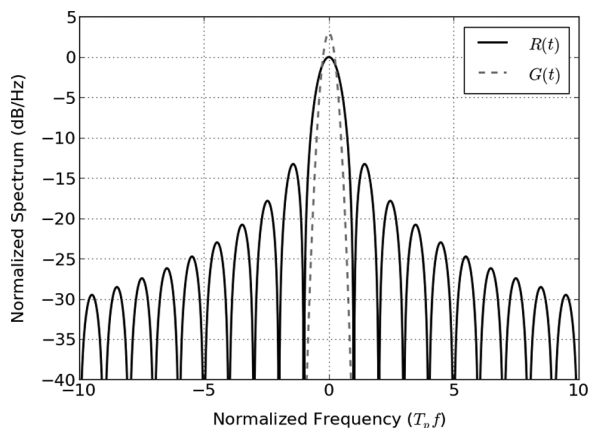

Fig. 3. Comparison of the spectra of $R(t)$ and $G(t)$ normalized to the peak power of $R(t)$. The spectrum of $G(t)$ is completely confined within the main lobe of $R(t)$ without any sidelobes. The rectangular pulse has spectral sidelobes 13 dB below the peak power and high out-of-band emissions.

a Gaussian output. The baseband signal is generated by an Agilent N8241A arbitrary waveform generator and up-converted to 10 GHz with an Agilent E8267D signal generator. The PA output signal is characterized with an Agilent N9030A signal analyzer, which has both time- and frequency-domain capabilities.

Fig. 3 illustrates the spectral benefit of using a Gaussian envelope compared to a rectangular pulse. A Gaussian pulse contains all of its power within a single main lobe and is more suited to fit inside an RSEC mask than a rectangular pulse with high sidelobes. The Gaussian pulse shape is given by

$$g(t) = \frac{1}{\sqrt{2\pi\sigma^2}} e^{\frac{-(t-\mu)^2}{2\sigma^2}} \qquad (1)$$

where μ is the mean, σ is the standard deviation, and it is normalized so that the integral of the pulse from minus to positive infinity is one. Since the Gaussian expands to infinity in both directions, it is not technically a pulse. We therefore modify the definition to

$$G(t) = \begin{cases} A_1 e^{\frac{(32t/4.51T_p)^2}{32}}, & |t| < 4.51\frac{T_p}{2} \\ 0, & \text{otherwise} \end{cases} \qquad (2)$$

where A_1 is a scalar describing the maximum pulse voltage amplitude and T_p is the pulse width of the rectangular pulse $R(t)$. The Gaussian pulse is 4.51 times wider than the rectangular pulse so that it has the same total energy as the rectangular pulse, ensuring similar range performance. The pulse is centered around zero (i.e., $\mu = 0$), and is chosen somewhat arbitrarily to fit four standard deviations within the pulse, containing 99.95% of the total energy of (1).

Section II discusses PA behavior under amplitude-modulated pulse operation and motivates the PA design used in experiments and simulations. Section III details the desired amplitude modulated waveform properties and tradeoffs. Section IV describes the design of the supply modulator that gives the desired waveforms. Finally, Section V gives results on an X-band monolithic microwave integrated circuit (MMIC) PA with supply-modulated chirped pulse waveforms.

II. PA Efficiency for a Gaussian Pulse

This section shows the theoretical efficiency for two classes of amplifiers under variable amplitude signal operation and a path to efficiency improvement. Typical radar PAs are biased in Class C for two reasons, which are: 1) it is a very efficient mode of operation and 2) it is a self-biasing topology [1], meaning the pulse turns on the amplifier and there is no current draw between pulses. Biasing below the transistor pinchoff voltage, as is done with Class C, results in high efficiency for rectangular pulses, but is not suitable for amplitude-modulated pulses.

To understand the effects of using a Class-C amplifier, consider an ideal amplifier, similar to what is described in [7], that has a drain current

$$\begin{aligned} i_d(t) &= g_m \left(V_B + V_1 \cos(\omega t)\right), \left(V_B + V_1 \cos(\omega t)\right) >= 0 \\ &= 0, \left(V_B + V_1 \cos(\omega t)\right) < 0 \end{aligned} \qquad (3)$$

where V_B is the dc bias voltage applied to the gate, V_1 is the amplitude of the fundamental voltage at frequency ω, and g_m is the transconductance. For the sake of simplicity, we assume that $i_d(t)$ is normalized to the maximum current, $I_{\max}$, and $g_m = 1$ A/V. Fig. 4 shows the Gaussian envelope current of a PA biased progressively deeper into cutoff. Decreasing V_B, thus biasing lower in Class C, results in sharper tails for the Gaussian pulse. This is undesirable distortion, which also degrades the spectrum.

Since Class C is not viable for waveforms with Gaussian envelopes, we show the impact of amplifier class on efficiency for Class A and Class B. Consider the definition of drain efficiency

$$\eta = \frac{P_L}{P_{DC}} = \frac{I_1^2 R_L}{2V_{DD}I_0} \qquad (4)$$

where I_1 is the magnitude of the RF current at the fundamental frequency, R_L is the load resistance and is set to the Class-A and Class-B optimal values of $V_{\max}/I_{\max}$, V_{DD} is the drain supply voltage, and I_0 is the average drain current [9]. For a Class-A PA bias, the quiescent drain current and voltage are $I_{DC} = I_{\max}/2$
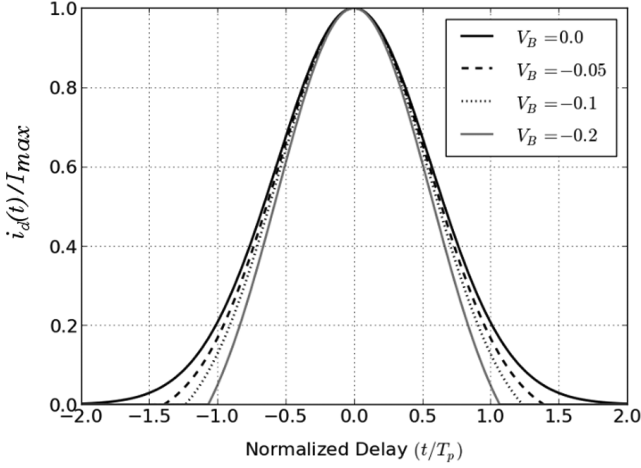
Fig. 4. Shape of the output Gaussian pulse from an amplifier biased at or below pinchoff. The Gaussian shape is perfectly maintained in Class B ($V_B = 0$ V, $V_1 \leq 1$ V). As the bias voltage is more negative, the tails of the Gaussian become sharper and thus distort the pulse. The pulse is normalized to the pulse width, T_p, of a rectangular pulse containing the same energy.
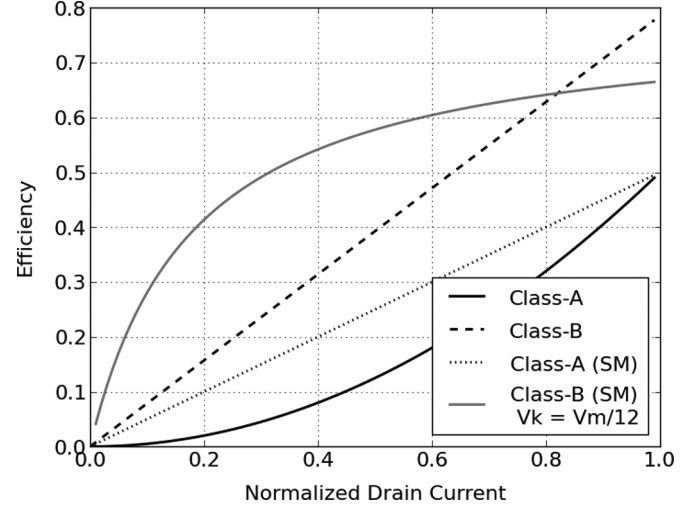

Fig. 5. Efficiencies of amplifier classes as a function of envelope current normalized to maximum fundamental current amplitude for the class (i.e., $I_{\max}/2$ for Class A and $I_{\max}$ for Class B). Both constant-supply and supply-modulated (SM) conditions are shown. The supply-modulated Class-B PA includes the losses associated with the knee voltage so it does not reach the theoretical peak efficiency of a Class-B PA at peak amplitude.

and $V_{DC} = V_{\max}/2$, respectively. The efficiency for any envelope can be found by substituting

$$I_0(A) = \frac{1}{T} \int_0^T \left[A \sin\left(\frac{2\pi t}{T}\right) + \frac{I_{\max}}{2} \right] dt = \frac{I_{\max}}{2} \quad (5)$$

and

$$I_1(A) = \frac{2}{T} \int_0^T \left[A \sin\left(\frac{2\pi t}{T}\right) \sin\left(\frac{2\pi t}{T}\right) \right] dt = A \quad (6)$$

into (4), where A is the current envelope amplitude. The result is

$$\eta_{\text{Class} A}(A) = \frac{2A^2}{I_{\max}^2}, \qquad \text{for } 0 \leq A \leq \frac{I_{\max}}{2}. \quad (7)$$

The same procedure can be followed for Class B to obtain

$$I_0(A) = \frac{1}{T} \int_0^{\frac{T}{2}} A \sin\left(\frac{2\pi t}{T}\right) dt = \frac{A}{\pi} \quad (8)$$

$$I_1(A) = \frac{2}{T} \int_0^{\frac{T}{2}} \left[A \sin\left(\frac{2\pi t}{T}\right) \sin\left(\frac{2\pi t}{T}\right) \right] dt = \frac{A}{2} \quad (9)$$

and

$$\eta_{\text{Class} B}(A) = \frac{A\pi}{4 I_{\max}}, \qquad \text{for } 0 \leq A \leq I_{\max}. \quad (10)$$

These results show that Class-A amplifier efficiency decreases quadratically with decreased amplitude while the Class-B efficiency only decreases linearly. Both of these classes have their dc voltages set for the maximum output power. If both classes of PAs had an adjustable voltage supply that allows for full voltage swing at a particular power level, it would result in a decrease in consumed dc power, and thus an improvement in efficiency. This adjustable supply voltage can be expressed as

$$V_{DD} = I_1(A) R_L \quad (11)$$

and substituted into (4) find efficiencies

$$\eta_{\text{Class} A \, (\text{SM})}(A) = \frac{A}{I_{\max}}, \qquad \text{for } 0 \leq A \leq \frac{I_{\max}}{2} \quad (12)$$

$$\eta_{\text{Class} B \, (\text{SM})}(A) = \frac{\pi}{4}, \qquad \text{for } 0 \leq A \leq I_{\max} \quad (13)$$

where subscript (SM) indicates supply modulation and the efficiency does not include any losses of the supply modulator. The Class-A amplifier is improved by envelope tracking in that its efficiency decreases linearly with amplitude, but the maximum remains at 50%. The Class-B ideal efficiency always remains at 78%; however, this does not include the impact of the knee voltage of the transistor. When the knee voltage, V_k, is taken into account, the efficiency becomes

$$\eta_{\text{Class} B \, (\text{SM})}(A) = \frac{\frac{V_{\max} - V_k}{8} A}{\frac{V_{\max} - V_k}{2\pi} A + \frac{V_k I_{\max}}{\pi}}. \quad (14)$$

In the TriQuint 150-nm GaN on a SiC process used for experimental demonstration in this paper, the knee voltage is between 3 and 4 V and the nominal drain supply voltage is 20 V, resulting in $V_{\max} = 40$ V. The efficiencies of these four modes of operation are shown as a function of signal amplitude in Fig. 5 and can be calculated over the duration of a Gaussian pulse, as shown in Fig. 6. The efficiency plotted in Fig. 6 shows the instantaneous efficiency, which penalizes the Class-B PA for low signal levels even though little dc power is being used. For this reason, it is helpful to calculate the average efficiency of the pulse, which factors in the total output power and total supplied power and is defined as

$$\eta_{\text{pulse}} = \frac{\int_{-T_p'}^{T_p'} I_1(G(t))^2 R_L \, dt}{\int_{-T_p'}^{T_p'} 2 V_{DD}(G(t)) I_0(G(t)) \, dt} \quad (15)$$

where $T_p' = (4.51 T_p)/(2)$. The pulse efficiency metric calculates the average output power over average dc power for the
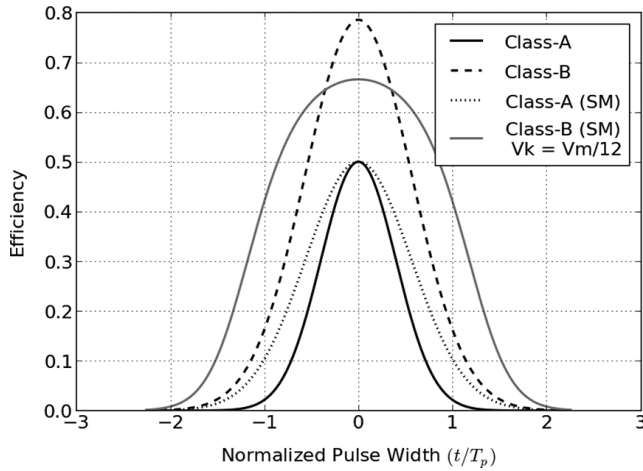
Fig. 6. Instantaneous efficiencies of amplifier classes over the duration of a Gaussian pulse.
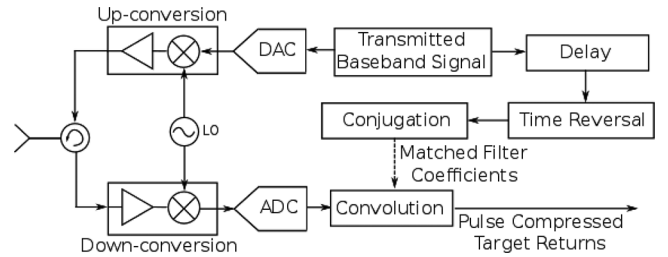

Fig. 7. Block diagram describing how waveforms are processed in a radar receiver. The baseband receive signal is convolved with the delayed time-reversed conjugated transmitted waveform. This process is known as matched filtering.
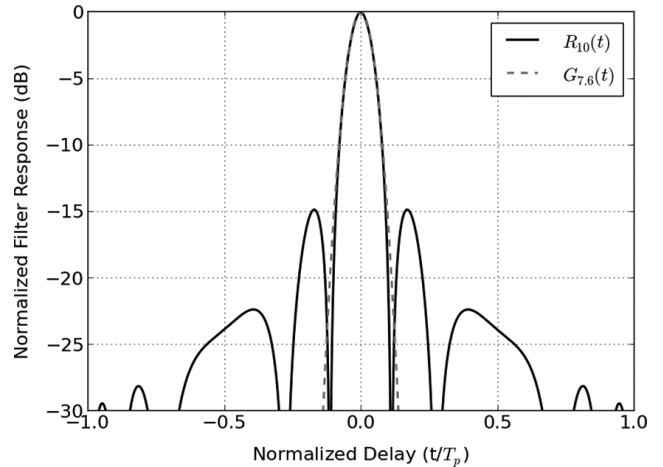

Fig. 8. Range resolution for both $R_{\beta T_p}(t)$ and $G_{\beta T_p}(t)$ with $\beta T_p = 10$ and $\beta T_p = 7.6$, respectively. Both achieve a tenfold improvement over $R(t)$ with the same T_p, but the Gaussian chirp does not have the time sidelobes. In range resolution plots, the time scale can be converted to meters by multiplying with $T_p c/2$.

entire pulse and is 11.1% for Class A, 15.7% for SM Class A, 55.5% for Class B, and 62.6% for SM Class B. This shows improvement in the efficiency for the Class-B cases, which do not use dc power when there in no output power. This analysis motivated our choice of a Class-B MMIC PA used in the validation experiments in Section V.

III. RADAR PULSE WAVEFORM DESIGN

The Gaussian-like pulse defined in (2) can be modified to include frequency modulation. The modulation used in this work is linear frequency modulation (LFM), also known as a chirp, which sweeps the immediate frequency from below to above the center frequency [10]. The frequency can also be swept down, but an up-chirp is used for this research. The baseband center frequency is zero, and shifts to the carrier frequency when up-converted. The definition of this waveform is

$$C_{\beta T_p}(t) = f(t) e^{\frac{j\pi \beta t^2}{T_p}} \qquad (16)$$

where β is the chirp bandwidth in hertz. The chirp is defined from negative to positive infinity and relies on $f(t)$ to limit its energy. For this work, $f(t)$ is either a rectangular pulse or Gaussian pulse, and β is the bandwidth swept within T_p. The convention here is to define the waveform as either $R_{\beta T_p}(t)$ or $G_{\beta T_p}(t)$, where the name specifies the envelope and βT_p defines the unitless time-bandwidth product. The presence of the chirp broadens the main lobe of the waveform spectrum proportionally to the value of βT_p.

FM is used in radar to improve the range resolution, which is a measure of how well closely spaced targets can be separated, and is calculated at the output of the receive filter. Range resolution can be deduced as the time between the half-power points of the receiver matched filter response, where received signals are filtered by $h(t)$ with the convolution integral

$$s_o(t) = \int_{-\infty}^{\infty} s(\tau) h(t - \tau) d\tau. \qquad (17)$$

In the above equation, $s(t)$ and $s_o(t)$ are the input and output signals of the filter, which is described as

$$h(t) = K s^*(t_0 - t) \qquad (18)$$

where K is a a constant, $(^*)$ is the conjugation operator, and t_0 is the two-way propagation delay to the target. The matched filter can be thought of as a delayed mirror image of the transmitted signal [11]. A high level block diagram of a radar is shown in Fig. 7 to illustrate the matched filter process. The transmitted baseband waveform is delayed, time-reversed, conjugated, and convolved with the received signal to generate the matched filter response.

By using a chirp, a rectangular pulse can achieve a tenfold increase in range resolution for $\beta T_p = 10$ since range resolution is proportional to the time-bandwidth product. Likewise, a Gaussian chirp can achieve the same range resolution using only $\beta T_p = 7.6$, as shown in Fig. 8. However, unlike for the rectangular pulse, the matched filter response of the Gaussian chirp does not have time sidelobes, which are undesirable artifacts of digital processing. Time sidelobes are problematic because they can create false target returns or mask true targets with lower power levels. Fig. 9 shows the βT_p required for decreasing range resolution requirements for both $R_{\beta T_p}(t)$ and $G_{\beta T_p}(t)$. For values of $\beta T_p > 5$, the ratio of the range resolution for the rectangular to Gaussian envelopes is about 1.3: 1.

The spectra of $R_{10}(t)$ and $G_{7.6}(t)$ are compared in Fig. 10. It is clear that the Gaussian envelope has the superior spectrum because it is contained in the main lobe without spectral spreading. From this analysis, one can conclude that a Gaussian shaped chirped pulse can be designed to match the performance of a
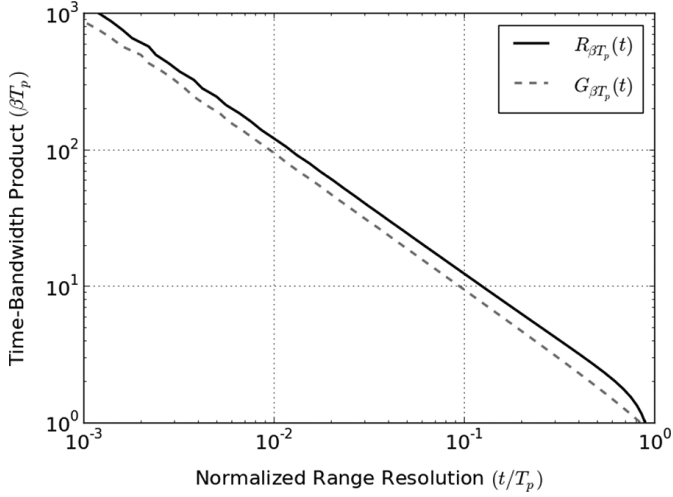
Fig. 9. Bandwidth needed for the rectangular and Gaussian chirped pulses for given range resolutions normalized to the range resolution of an unmodulated rectangular pulse of width T_p. The Gaussian always has a better range resolution for a given βT_p and the ratio of rectangular to Gaussian resolution is about 1.3:1.
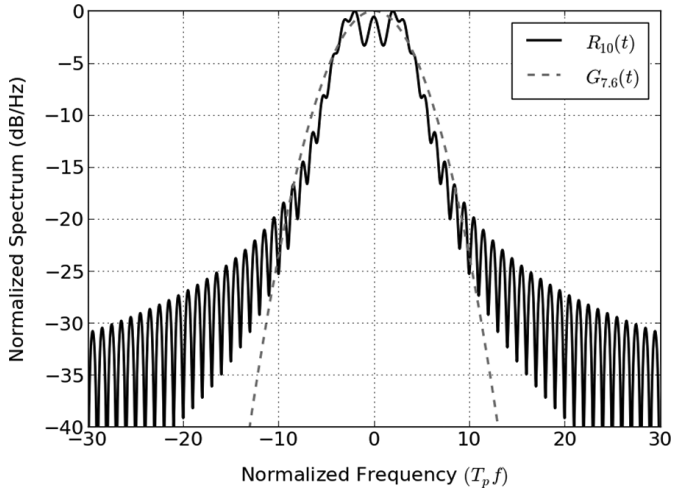

Fig. 10. Calculated spectra of $R_{10}(t)$ and $G_{7.6}(t)$. Both provide a tenfold improvement in range resolution over $R(t)$ while maintaining the same energy.

chirped rectangular pulse in both the energy and range resolution, while demonstrating a dramatic improvement in spectral quality. This analysis assumed that A_1 is aligned with the peak power of the PA. Therefore, longer pulses must be used if more signal-to-noise ratio is desired. An increase in β would need to accompany the wider pulse to ensure the same time-bandwidth product and range resolution. A supply modulator can be used to produce $G_{\beta T_p}(t)$ in an efficient manner, as shown in Section II, resulting in improved spectral properties while similar in signal-to-noise ratio and range resolution to $R_{\beta T_p}(t)$.

IV. RESONANT SUPPLY MODULATOR

Supply modulation of RF PAs has recently been applied in envelope tracking transmitters, e.g., [12] and [13], or to improve operation of outphasing [14] and Doherty PAs [15], [16], with a primary goal to improve transmitter efficiency for high peak-to-average ratio signals. In these architectures, the supply

modulation is typically done with an efficient switching dc–dc converter assisted with a linear amplifier that provides the required bandwidth [17]. In principle, this approach can be applied to radar transmitters to generate the Gaussian-type amplitude envelope modulation described in Section III. However, supply modulators applied to communication signals with high peak-to-average power ratios (PAPRs) typically cover amplitude values from some $V_{\min}$ to $V_{\max}$, where $V_{\min} > 0$. In the radar case, the envelope goes to zero between pulses, and the envelope waveform is known *a priori*. A simpler approach, which is also potentially more efficient compared to a more standard envelope modulator, is a supply modulator based on a damped resonant circuit, first demonstrated in [18] and [19]. In [18], a 15-μs pulse with an approximately Blackman shape (PAPR = 4 dB) and with no frequency modulation was applied to a 2-GHz PA and showed about ten-point improvement in efficiency over a directly driven PA. The modulator in [19] exhibits a very high efficiency of 90% at 20-V peak voltage.

In this work, we modify the resonant modulator approach to enable variable width pulses with widths in the 5–10-μs range and with 10-W power. The circuit diagram is shown in Fig. 11(a), where the switches $S_{1,2}$ are used to shape the pulse and S_3 turns the pulse off. The modulator circuit has the following three different states.

1) S_1 closed and the other two open; this can be thought of as the charging configuration since it is providing energy to the circuit via V_D.
2) The discharging state in which V_D is disconnected from the circuit by opening S_1 while closing S_2. This state essentially replaces V_D with a zero volt source, or short circuit.
3) The "off" state, with S_2, S_3 closed and S_1 open. This state is similar to State 2) in that it disconnects the source, but the purpose is to remove energy from the circuit as quickly as possible. It is used at the end of a resonant pulse and the circuit is left in this state between pulses.

The schematic for States 1) and 2) can be simplified to what is shown in Fig. 11(b), where R represents the load presented by the PA and R_p are parasitic resistances in the switches and lumped elements. The source $V = V_D \neq 0$ in State 1) and $V_D = 0$ in State 2). The modulator is operated by cycling from State 1) to State 2) at t_1 and back to State 1) at t_2. At T_p, the circuit is put in State 3) between pulses. The remainder of this paper deals with Gaussian-shaped pulses exclusively so T_p assumes the $4.51T_p$ scaling to the rectangular pulse.

The drain voltage and inductor current in Fig. 11(b) can be written as

$$v_{dd}(t) = V_D - i_L(t)R_p - \frac{di_L}{dt}L \quad (19)$$

and

$$i_L(t) = \frac{dv_{dd}(t)}{dt}C + \frac{v_{dd}(t)}{R}. \quad (20)$$

The solution to (19) can be written as

$$v_{dd}(t) = e^{-\omega_0 t/2Q}\left(A\cos(a\omega_0 t) + B\sin(a\omega_0 t)\right) + V_D \quad (21)$$

where $\omega_0 = 1/\sqrt{LC}, Q = 1/((R_p)/(\zeta) + (\zeta)/(R)), a = \sqrt{1 + (R_p/R) - (1/2Q)^2}$ with $\zeta = \sqrt{L/C}$ and $V_D = 0$ in State 2). Note that lower values of the Q factor result in lower
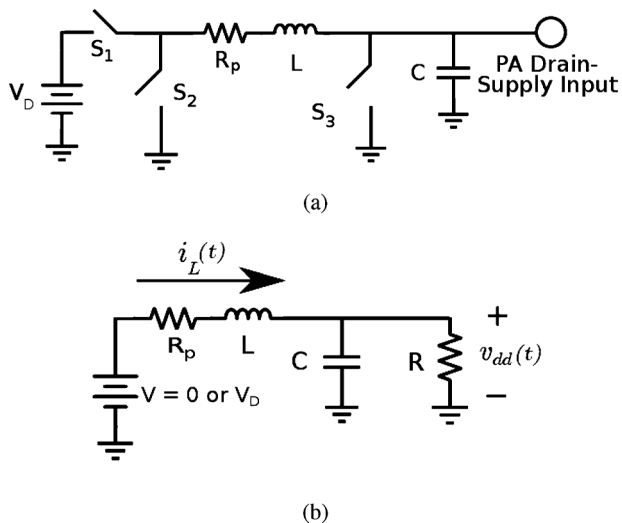
(a)

(b)

Fig. 11.   (a) Schematic of the resonant modulator circuit. The circuit uses the resonance of the inductor and capacitor to shape the waveform applied to the drain of a PA. Switches S_1 and S_2 are used to connect and disconnect the voltage source. S_3 is used to discharge the circuit when the modulator is not in use. (b) Equivalent circuit for State 1)—S_1 closed, and State 2)—S_2 closed.
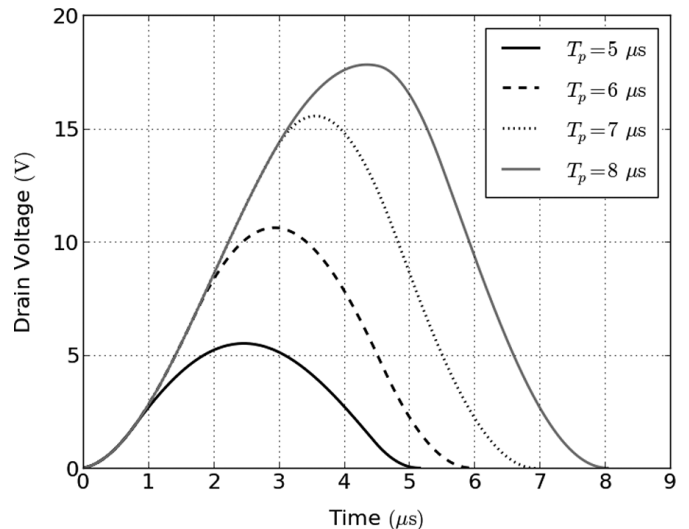

Fig. 12.   Varying-length Gaussian-like pulses obtained by optimization of the switching times. If the circuit elements are kept constant, the decreasing resonant modulator pulse duration comes at the expense of peak voltage. The switching times required are shown in Table I.

TABLE I
IDEAL SWITCHING TIMES FOR PULSES IN FIG. 12

T_p (μs)	t_1 (μs)	t_2 (μs)	t_3 (μs)
5.0	0.8	4.5	5.2
6.0	1.7	4.6	6.0
7.0	2.9	4.8	6.9
8.0	4.5	5.5	8.0

current peaks, and thus lower losses in R_p. The coefficients A and B are solved numerically, subject to boundary conditions of continuous v_{dd} and its first derivative (soft switching), and separately for the three states. The solution for the pulse waveform can now be written as

$$
v_{dd}(t, t_1, t_2)
= \begin{cases}
-e^{-\omega_0 t/2Q} V_D(a\omega_0 t) + V_D \\
\quad : 0 < t < t_1 \\
e^{-\omega_0 t/2Q} \left(A_2 \cos(a\omega_0 t) + B_2 \sin(a\omega_0 t) \right) \\
\quad : t_1 < t < t_2 \\
e^{-\omega_0 t/2Q} \left(A_3 \cos(a\omega_0 t) + B_3 \sin(a\omega_0 t) \right) + V_D \\
\quad : t_2 < t < T_p
\end{cases}
\tag{22}
$$

where A_2 and B_2 are dependent on t_1 and A_3 and B_3 are dependent on t_2.

To solve for a Gaussian shape, a criterion for optimization is established by defining times $t_{\max}$ and t_{end} when $v_{dd}(t, t_1, t_2)$ is at its maximum and minimum values, respectively, and where the minimum value is at the end of the pulse. These times are not to be confused with t_1 and t_2, which specify the times when the states change. The following three conditions need to be satisfied:

$$
v_{dd}(t_{\mathrm{end}}, t_1, t_2) = 0 \tag{23}
$$

$$
t_{\mathrm{end}} = 2 t_{\max} \tag{24}
$$

$$
t_{\mathrm{end}} = T_p \tag{25}
$$

where T_p is the desired pulse width. To find t_1 and t_2, which best meet (23)–(25), we examine the set of all $v_{dd}(t, t_1, t_2)$, where $0 \le t_1 \le t_2 \le T_0 = 2\pi\sqrt{LC}$ and apply the cost function

$$
J(v_{dd}(t_{\mathrm{end}}, t_1, t_2)) = |v_{dd}(t_{\mathrm{end}}, t_1, t_2)|
$$

$$
+ |t_{\mathrm{end}} - 2 t_{\max}| + |t_{\mathrm{end}} - T_p| \tag{26}
$$

to find the set member, which minimizes the scalar $J(v_{dd}(t_{\mathrm{end}}, t_1, t_2))$. Strictly, $t_{\max}$ and t_{end} should be the roots

of $dv_{dd}(t_{\mathrm{end}}, t_1, t_2)/dt$, but they do not always exist as analytical solutions, and are here found numerically. The results of this method are shown in Fig. 12 for a circuit using the following values: $L = 20$ μF, $C = 100$ nF, $R = 220$ Ω, $R_p = 0.8$ Ω, and $V_D = 10$ V. These results show that Gaussian-like pulses can be created with the switched resonant circuit. Additionally, this method allows for the design of pulses where $T_p \le T_0$. The shorter pulse width comes at the expense of peak voltage, but this extra degree of freedom is useful when the supply modulator is connected to a PA, as discussed in Section V.

The circuit is implemented in the NI/AWR Microwave Office circuit simulator, with switch controls generated at the system level in Virtual System Simulator (VSS). The same values of L, C, and R as above are used, it is assumed that the reactive elements are lossless, and the losses R_p are taken into account with the SPICE model of NDF08N60ZG power MOSFETs used to implement the switches. For a 7-μs pulse, the times obtained by optimization result in the waveform shown in Fig. 13 in blue (in online version), which does not return to zero at the end of the pulse until the circuit is in State 3). When the switching times are adjusted to account for parameters that were neglected before, such as parasitics of the reactive elements, $t_2 = 5.08$ μs is increased by 17% and $t_{\mathrm{end}} = 6.78$ μs is decreased by 1%, resulting in the adjusted waveform in Fig. 13.

In the circuit simulation, modulator efficiency is measured over the pulse duration as

$$
\eta = \frac{\int_0^{T_p} v_{\mathrm{load}}(t) i_{\mathrm{load}}(t) dt}{\int_0^{T_p} V_{\mathrm{in}} i_{\mathrm{in}}(t) dt} \tag{27}
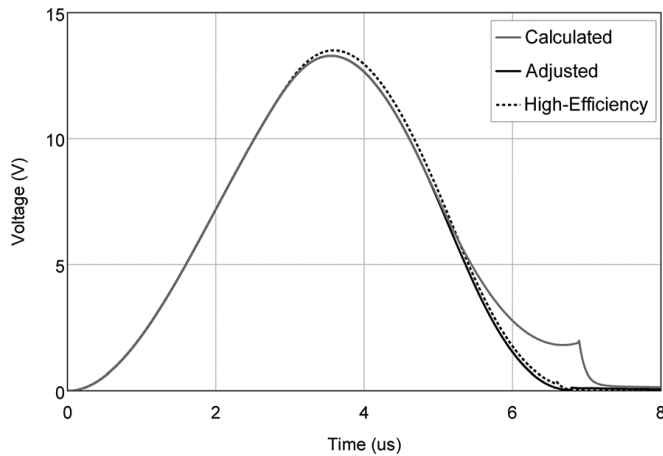$$

Fig. 13. Resulting $v_{dd}(t)$ waveform for a resonant modulator simulated in AWR with spice switch models. The nonideal characteristics of the switches change the output waveform shape so the switching times are adjusted to correct the shape. The black trace shows that the waveform shape can be preserved even when there is an off time between transitions when both S_1 and S_2 are off to avoid shorting the voltage source.
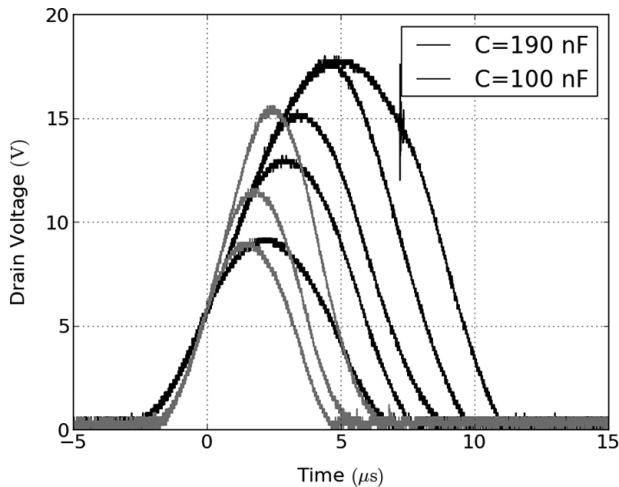

Fig. 14. Measured output pulse shape for two values of C into a static 220-Ω load. For each pulse, t_1 and t_2 are changed.

where $v_{\text{load}}(t)$ and $i_{\text{load}}(t)$ are measured at the resistive load R of the modulator, while V_{in} and $i_{\text{in}}(t)$ are measured at the voltage source supplying the modulator.

The resulting efficiency for this simulation is only 19% due to high current spikes during switching times when the input voltage source is shorted. By introducing 250-ns dead times during switching, the simulated efficiency improves to 83.4%. The resonant supply modulator is implemented with $L = 22$ nH and a dual-switched capacitor $C = 100$ nF and $C = 190$ nF, included to demonstrate how pulse width can be digitally modified. Measured results into a static 220-Ω load are shown in Fig. 14 and summarized in Table II. The measured efficiencies here serve to confirm modulator functionality since the PA drain supply impedance is not expected to behave like a constant resistive load.

V. SUPPLY-MODULATED MMIC PA

Simulations were performed in AWR VSS using the circuit envelope simulator with a 4-W GaN X-band MMIC biased in

TABLE II
SUMMARY OF MODULATOR MEASUREMENTS WITH $R = 220\ \Omega$

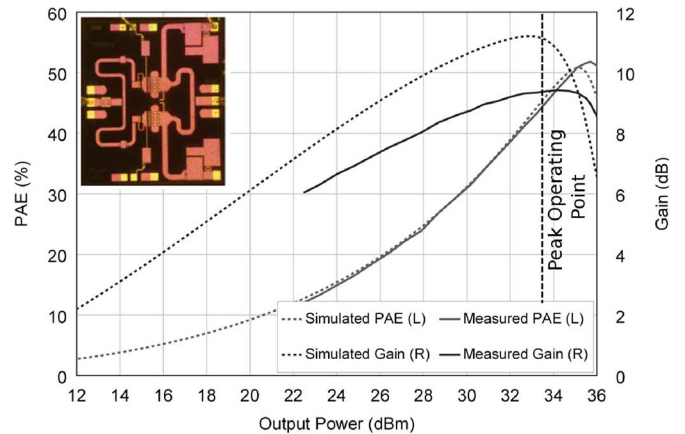| T_p (μs)	Measured T_p (μs)	Capacitance (nF)	Peak Voltage (V)	Efficiency
7.0	6.9	100	9.2	51.2%
8.0	8.0	100	11.6	57.3%
9.0	9.1	100	15.6	64.1%
10.0	9.9	190	9.4	40.8%
11.0	10.6	190	13.2	45.8%
12.0	12.1	190	15.4	52.4%
13.0	13.0	190	18.0	59.3%
14.0	14.0	190	18.0	55.2%

Fig. 15. Simulated output power sweep for 4-W MMIC PA used in simulation and measurement. The peak PAE is 50.8% at 35.2-dBm output power. The peak gain is 11.2 dB and the gain is 9.5 dB at peak efficiency.
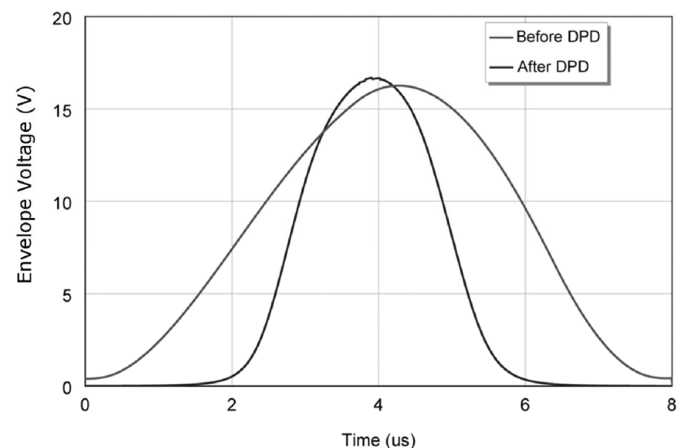

Fig. 16. RF PA envelope voltage for both before and after DPD is applied. The desired 4σ pulse width is 8 μs.

Class B. The measured continuous wave (CW) performance of the single-stage 2.0×2.3 mm MMIC PA is published in [20], and harmonic balance circuit simulation results with a TriQuint nonlinear model are shown in Fig. 15. The peak power-added efficiency (PAE) is 50.8% at 35.2-dBm output power. The peak gain is 11.2 dB, and drops to 9.5 dB at peak efficiency.

VSS circuit envelope simulations were performed in two configurations: amplifying a Gaussian LFM with a constant supply and amplifying it with the resonant modulator. The constant supply simulations applied an 8 μs Gaussian pulsed LFM with 5 MHz of bandwidth to the PA input. In both simulations we

tried to achieve a peak pulse power of 33.5 dBm because this is the location of peak gain so the amplifier was not compressed and operated in Class B. To quantify how close the RF output is to a Gaussian pulse given by (12), the following metric is used to measure the error:

$$\epsilon = \sqrt{\frac{\int_0^{T_p} \left(|v_{\text{loadPA}}(t)| - |v_{\text{desired}}(t)|\right)^2 dt}{\int_0^{T_p} |v_{\text{desired}}(t)|^2 dt}} * 100 \qquad (28)$$

where $v_{\text{loadPA}}(t)$ is the complex baseband PA load voltage and $v_{\text{desired}}(t)$ is the time-aligned desired load voltage when the input voltage is linearly scaled. The constant supply simulation achieves an $\epsilon = 11.8\%$ without any pre-distortion. The supply-modulated simulations are done in two steps. First, a rectangular LFM is applied to the input of the PA with the resonant modulator adjusted to an 8-μs pulse and connected to the drain supply input of the PA for direct polar modulation. The resulting waveform, shown in Fig. 16, had an $\epsilon = 65.8\%$ so digital pre-distortion (DPD) is needed. In this case, element-wise division is used to solve for he appropriate scaling factor, which is then applied to the rectangular input waveform to shape the envelope and improve the error to $\epsilon = 12.8\%$. Thus, the resonant modulator does some shaping of the pulse by adjusting PA gain, but additional amplitude modulation to the input pulse is required to lower total error.

The magnitudes of the RF PA load voltages are shown in Fig. 17. For the constant-supply PA, a chirped Gaussian pulse is applied to the PA input. For the supply-modulated PA, the resonant voltage is applied to the drain supply and the pre-distorted chirped rectangular pulse is applied to the PA input. Both are compared to the desired output waveform. Fig. 18 shows the output spectra of the amplified signals. The spectra of the amplified signals are broader than the desired spectrum, but do not have sidelobes and have properties that would comply with the regulations of Fig. 1. The modulated PA does have higher out-of-band emissions than the constant supply case, but they are 70 dB below the peak power.

The results from simulations are summarized in Table III. Use of the resonant modulator provided an increase of ten points in efficiency over a constant supply. The definitions for efficiencies quoted in Table III are the PAE

$$\text{PAE} = \frac{\int_0^{T_p} |v_{\text{loadPA}}(t)|^2 - |v_{\text{inPA}}(t)|^2 dt}{2 Z_{\text{load}} \int_0^{T_p} v_{dd}(t) i_d(t) dt} \qquad (29)$$

and composite power-added efficiency (CPAE)

$$\text{CPAE} = \frac{\int_0^{T_p} |v_{\text{loadPA}}(t)|^2 - |v_{\text{inPA}}(t)|^2 dt}{2 Z_{\text{load}} V_{dd} \int_0^{T_p} i_{\text{supply}}(t) dt} \qquad (30)$$

where $v_{\text{inPA}}(t)$ is the complex baseband voltage at the input to the PA, Z_{load} is the PA load impedance, $v_{dd}(t)$ and $i_d(t)$ are measured at the drain of the PA, and V_{dd} and $i_{\text{supply}}(t)$ are measured at the input to the supply modulator. CPAE includes
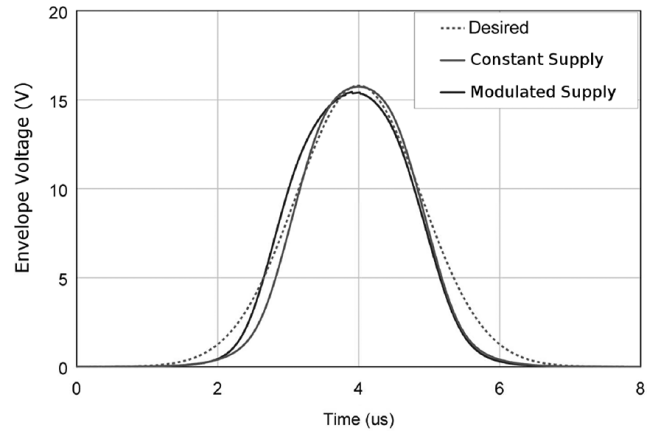

Fig. 17. Simulations show that a near Gaussian shape can be achieved at the output of the PA for a constant supply and Gaussian LFM, or a pre-distorted rectangular LFM.
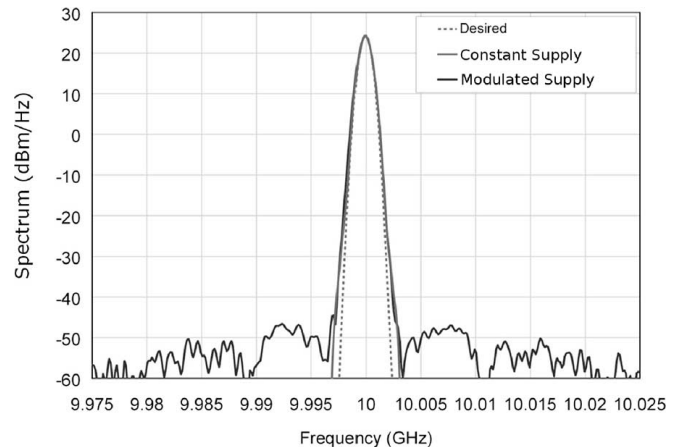

Fig. 18. Simulated spectra of the chirped Gaussian pulse for a constant supply and modulated supply. Both cases make the spectrum slightly broader, but still operate without sidelobes. The modulated case has out-of-band spurious emissions due to higher nonlinearities in the system, but they are 70 dB below the peak power, while the average efficiency is ten points higher.

TABLE III
SUMMARY OF RESONANT-MODULATED PA SIMULATIONS

	Constant Bias	Supply-Modulated
P_{max}	34.1 dBm	34.4 dBm
Average Pulse Power	420 mW	470 mW
Average Drain Pulse Power	1830 mW	1260 mW
PAE_{avg} (PAE_{max})	21% (40%)	33% (41%)
$CPAE$	21%	30%
Error	$\epsilon = 11.8\%$	$\epsilon = 12.8\%$

the losses of the modulator for the supply-modulated case, and is the same as PAE for constant supply since there is no modulator.

Measurements are performed on the same PA used in the simulations, but with a twofold increase in inductance and decrease in capacitance. The modulator was characterized using the setup shown in Fig. 19 with a pulsed gate voltage increased to the maximum available from the driver chips. This decreases the field-effect transistor R_{on} of the (FET) switches. A measurement of the modulator efficiency with the PA as a load and pulsed LFM input results in measured input and output powers shown
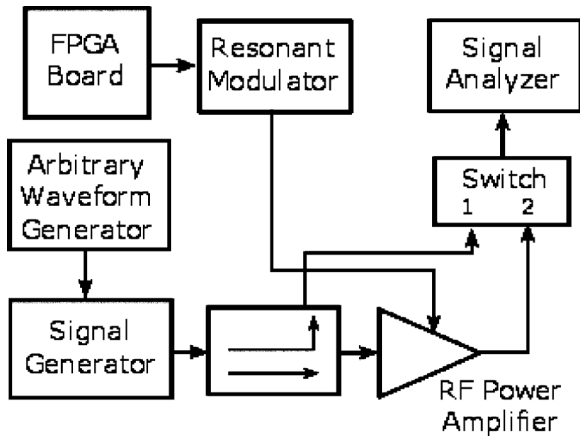
Fig. 19. Bench setup used for supply modulation measurements. The equipment includes an Altera DE2 field programmable gate array (FPGA) development board, an Agilent N8241A arbitrary waveform generator, an Agilent E8267D signal generator, and an Agilent N9030A PXA signal analyzer. The switch at the input of the signal analyzer allows for measuring either the input or the output of the RF PA.

Fig. 21. Comparison of the envelope voltage for the measured Gaussian-like pulses at the output of the PA. The constant supply pulse is close to a Gaussian with an error of $\epsilon = 10\%$ and the supply-modulated pulse has an error of $\epsilon = 12\%$.
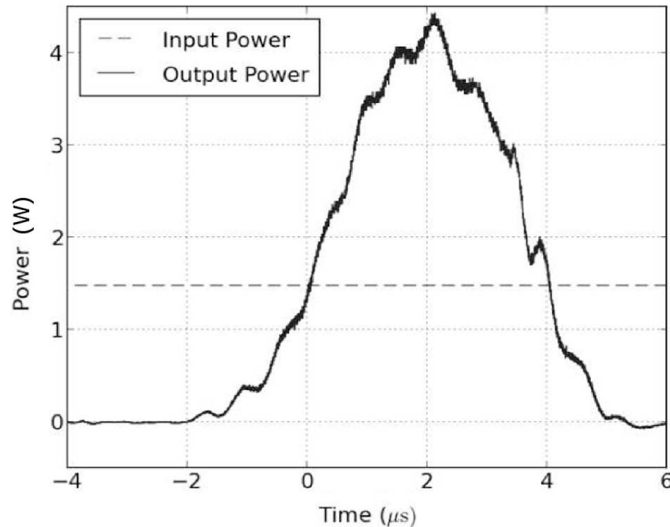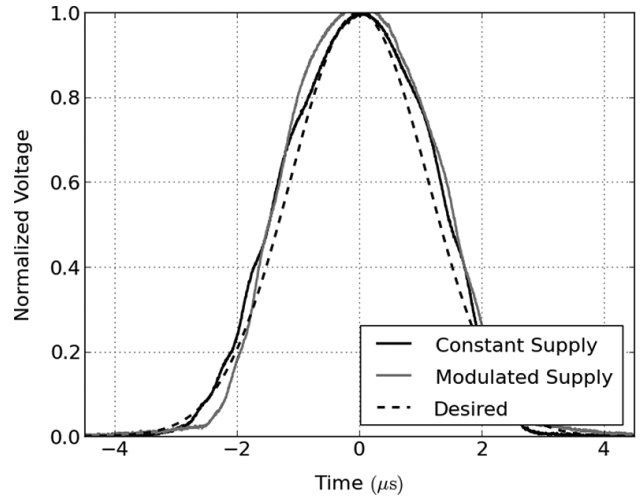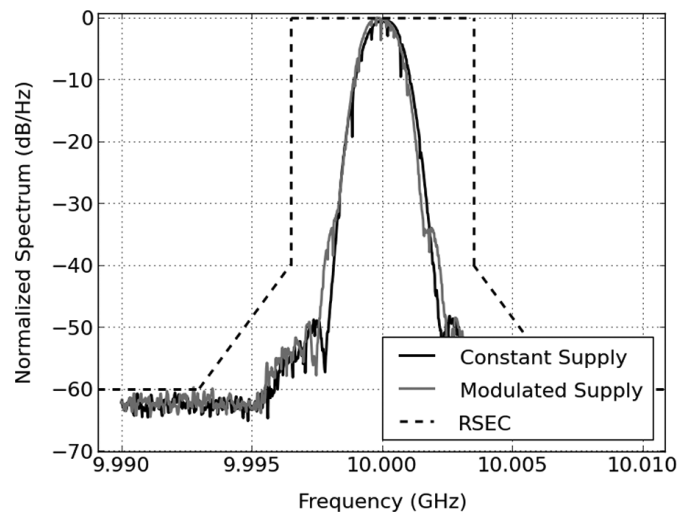

Fig. 20. Measurement of the input and output power of the supply modulator when connected to a PA with a pulsed Gaussian LFM waveform. With the PA as a load, the modulator demonstrates 92% average efficiency for this measurement. It is not possible to plot instantaneous efficiency due to the pulsed nature of this measurement and the multiple storage devices present in the circuit. The negative times correspond to the trigger used on the oscilloscope. Thus, the pulse at $t = 0$ is the one that triggered the oscilloscope.

Fig. 22. Measured spectra of the constant-supply and supply-modulated PA. Both fit within the NTIA RSEC for a 9-μs unmodulated rectangular pulse. One should note that a rectangular pulse with equivalent energy (9 μs) would have an even wider RSEC. Clearly, $G_{\beta T_p}(t)$ has no issues complying with the most stringent of RSEC.

in Fig. 20. The modulator efficiency achieved in this measurement when modulating a PA is 92%.

A comparison is next performed between the PA when operated with a constant and modulated supply for a 9-μs Gaussian pulse with 5 MHz of LFM bandwidth and a duty cycle of 10%. The amplifier is operated such that the peak output power of the Gaussian pulse would be about 32.5 dBm. This output power is chosen because it is the limit of the amplifier linear operation. If the amplifier were driven any harder, the top of the pulse would flatten due to saturation. Very little pre-distortion is needed in both cases. The only form of pre-distortion used in this case is to include fewer standard deviations in the Gaussian pulse at the input of the amplifier. This technique makes the input

pulse wider, but the lower gain of the amplifier at backed-off powers returns the pulse to its desired shape. Fig. 21 shows the output pulses from the constant supply and supply-modulated PA. When compared to the desired pulse with four standard deviations, both test cases have a similar shape. The spectra of the two test cases are shown in Fig. 22; both have the desirable spectral properties that conform with NTIA requirements, but the SM case has higher efficiency.

The measured baseband time-domain waveform of the supply-modulated PA is shown in Fig. 23 and the matched filter response for this waveform is shown in Fig. 24. This pulse has a range resolution of 80 m. More LFM bandwidth can be used to reduce range resolution within PA bandwidth restrictions, around 300 MHz for this PA. The time sidelobes of the matched
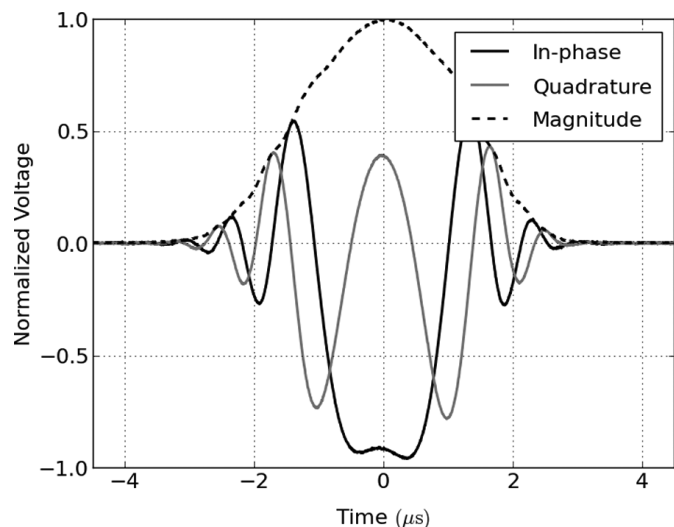
Fig. 23.   Measured baseband time-domain waveform of the supply-modulated PA. The 9-μs pulse has 5 MHz of LFM bandwidth and contains four standard deviations.

(a)

(b)

Fig. 25.   (a) Measured drain efficiencies of the constant-supply and supply-modulated PA. (b) Calculated power dissipated by the PA.
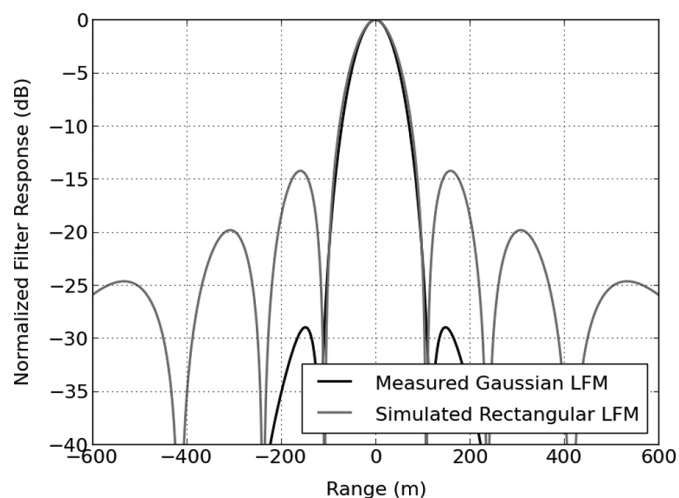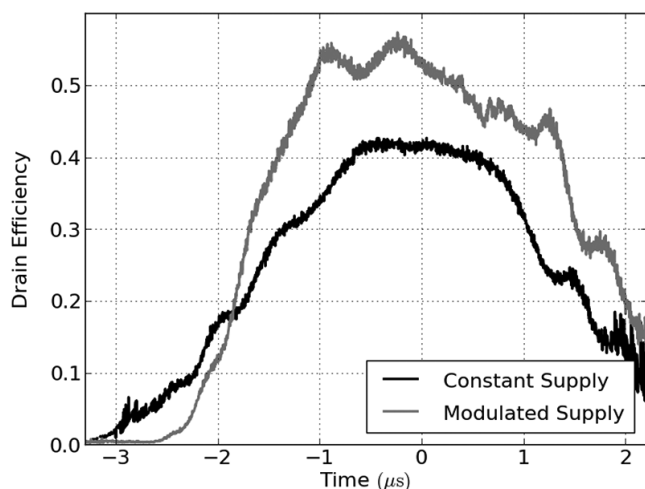

Fig. 24.   Matched filter response of supply-modulated PA. This particular pulse has a range resolution of 80 m, but more bandwidth could be used to improve upon this. The time sidelobes are 29 dB below the maximum.
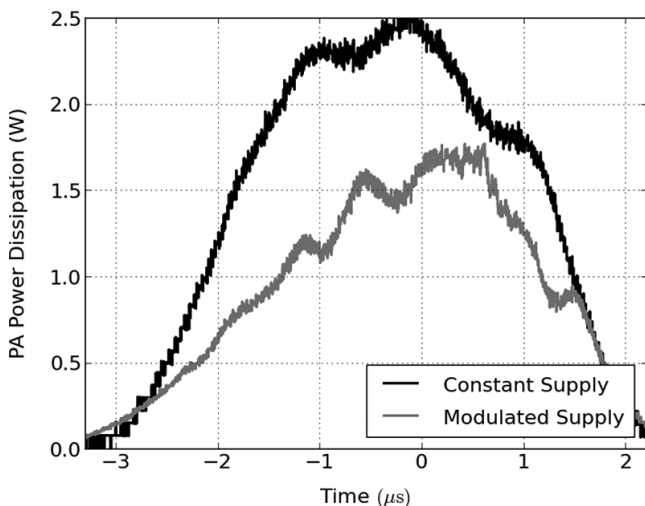
TABLE IV
SUMMARY OF RESONANT-MODULATED PA MEASUREMENTS

	Constant Bias	Supply-Modulated
P_{max}	32.5 dBm	32.7 dBm
Average Pulse Power	450 mW	470 mW
Average Drain Pulse Power	1170 mW	1040 mW
PAE_{avg} (PAE_{max})	34% (40%)	40% (55%)
$CPAE$	31%	36%
Error	$\epsilon = 10\%$	$\epsilon = 12\%$

filter response are 29 dB below the maximum response. This shows 14-dB improvement over the time sidelobes of $R_{\beta T_p}(t)$.

A summary of the efficiency measurements over a single pulse are shown in Table IV. The instantaneous drain efficiency is shown in Fig. 25(a) and the PA power dissipation is shown in Fig. 25(b). As in the case of simulations, this is lower than the theoretical limits derived in Section II, but is to be expected

because the maximum PAE is lower than that of an ideal Class-B amplifier.

VI.   CONCLUSION

We have demonstrated both theoretically and experimentally an efficient radar transmitter with improved spectral confinement, by shaping the pulse envelope to be close to a Gaussian. A simple variable-pulsewidth resonant supply modulator with an efficiency of 92% is connected to the drain supply input of a 4-W GaN X-band MMIC PA and results in 36% overall time-average system efficiency, a five-point improvement compared to the directly driven PA case. The theoretical investigation pointed to operating the PA in Class B, with a peak measured efficiency of 48% at 10 GHz, and an average PAE = 40% when supply modulation is used for pulse envelope modulation. The spectral emissions are reduced by 40 dB relative to the case of a rectangular pulse with the same energy as the Gaussian pulse. In addition to spectral confinement, a 5-MHz chirp bandwidth results in a range resolution of 80 m and the first time sidelobe

at -29 dB, a 15.5-dB improvement compared to the rectangular pulse shape. The range resolution can be reduced with a broader bandwidth chirp since the PA bandwidth is about 300 MHz.

Supply modulator efficiency can be further improved by using lower loss MOSFET switches, gate drivers with higher output voltages, and a decreased R_{on} and lower loss surface mount lumped element components, all of which are commercially available. Additionally, PA efficiency can be improved by using harmonically terminated heavily saturated PAs at the expense of more requirements on the DPD. The efficiency results presented here are for a single pulse and a single PA. In a phased array radar, a watt-level PA such as the one presented here is used at each element, and the efficiency improvement in an array and for many pulses will result in considerable power savings at the system level, with modest complexity increase due to the very simple and efficient supply modulator architecture. In summary, the work in this paper demonstrates that radar transmitters with amplitude-modulated pulses can dramatically reduce spectral emissions while maintaining high average efficiency.

REFERENCES

[1] M. Skolnik, *Radar Handbook: Third Edition*. New York, NY, USA: McGraw-Hill, 2008.
[2] *"Manual of Regulations and Procedures for Federal Radio Frequency Management,"* U.S. Dept. Commerce, NTIA, Washington, DC, USA, 2013.
[3] NBC News "FCC warns of mobile's looming spectrum crisis," Oct. 2009 [Online]. Available: http://www.nbcnews.com
[4] C. Baylis, M. Fellows, L. Cohen, and R. Marks, "Solving the spectrum crisis: Intelligent, reconfigurable microwave transmitter amplifiers for cognitive radar," *IEEE Microw. Mag.*, vol. 15, no. 5, pp. 94–107, Jul. 2014.
[5] J. A. J. de Graaf, H. Faust, and S. Talapatra, "Generation of spectrally confined transmitted radar waveforms: Experimental results," in *IEEE Radar Conf.*, Apr. 2006, pp. 8, 24–27.
[6] R. Chen and B. Cantrell, "Highly bandlimited radar signals," in *Proc. IEEE Radar Conf.*, 2002, pp. 220–226.
[7] E. McCune, "Operating modes of dynamic power supply transmitter amplifiers," *IEEE Trans. Microw. Theory Techn.*, vol. 62, no. 11, pp. 2511–2517, Nov. 2014.
[8] E. McCune, "Envelope tracking or polar—Which is it? [microwave bytes]," *IEEE Microw. Mag.*, vol. 13, no. 4, pp. 34–56, May 2012.
[9] S. C. Cripps, "Conventional high efficiency amplifier modes," in *RF Power Amplifiers for Wireless Communications*, 2nd ed. Norwood, MA, USA: Artech House, 2006, ch. 3, pp. 39–65.
[10] M. Richards, *Fundamentals of Radar Signal Processing*. New York, NY, USA: McGraw-Hill, 2005.
[11] N. Levanon and E. Mozeson, *Radar Signals*. New York, NY, USA: Wiley, 2004.
[12] D. E. A. Kimball, "High-efficiency envelope-tracking W-CDMA base-station amplifier using GaN HFETs," *IEEE Trans. Microw. Theory Techn.*, vol. 54, no. 11, pp. 3848–3856, Nov. 2006.
[13] J. Hoversten, S. Schafer, M. Roberg, M. Norris, D. Maksimovic, and Z. Popović, "Codesign of PA, supply, and signal processing for linear supply-modulated RF transmitters," *IEEE Trans. Microw. Theory Techn.*, vol. 60, no. 6, pp. 2010–2020, Jun. 2012.
[14] P. Godoy, D. Perreault, and J. Dawson, "Outphasing energy recovery amplifier with resistance compression for improved efficiency," *IEEE Trans. Microw. Theory Techn.*, vol. 57, no. 12, pp. 2895–2906, Dec. 2009.
[15] D. Kang, J. Choi, D. Kim, and B. Kim, "Design of Doherty power amplifiers for handset applications," *IEEE Trans. Microw. Theory Techn.*, vol. 58, no. 8, pp. 2134–2142, Aug. 2010.
[16] J. Choi, D. Kang, D. Kim, and B. Kim, "Optimized envelope tracking operation of Doherty power amplifier for high efficiency over an extended dynamic range," *IEEE Trans. Microw. Theory Techn.*, vol. 57, no. 6, pp. 1508–1515, Jun. 2009.
[17] C. H. *et al.*, "Digitally assisted dual-switch high-efficiency envelope amplifier for envelope-tracking base-station power amplifiers," *IEEE Trans. Microw. Theory Techn.*, vol. 59, no. 11, pp. 2943–2952, Nov. 2011.
[18] M. Roberg, M. Rodriguez, D. Maksimovic, and Z. Popović, "Efficient and linear amplification of spectrally confined pulsed AM radar signals," *IEEE Microw. Compon. Lett.*, vol. 22, no. 6, pp. 279–281, Jun. 2012.
[19] M. Rodriguez, M. Roberg, A. Zai, E. Alarcon, Z. Popović, and D. Maksimovic, "Resonant pulse-shaping power supply for radar transmitters," *IEEE Trans. Power Electron.*, vol. 29, no. 2, pp. 707–718, Feb. 2014.
[20] S. Schafer, M. Litchfield, A. Zai, Z. Popović, and C. Campbell, "X-band MMIC GaN power amplifiers designed for high-efficiency supply-modulated transmitters," in *IEEE MTT-S Int. Microw. Symp. Dig.*, Jun. 2013, pp. 1–3.

Andrew Zai (M'07) received the B.S. and M.S. degrees in electrical engineering from Virginia Polytechnic Institute and State University, Blacksburg, VA, USA, in 2007 and 2011, and the Ph.D. degree from the University of Colorado at Boulder, Boulder, CO, USA, in 2014. His M.S. thesis concerned adaptive interference cancellation in phased-array radars. He successfully defended his doctoral disseration on efficient power amplifiers for radar applications in 2014.

He was with the Department of the Navy within the Naval Acquisition Development Program. In early 2010, he finished with a Level II Systems, Planning, Research, Development, and Engineering (SPRDE) certificate. He then joined the Johns Hopkins Applied Physics Laboratory, Air and Missile Defense Department, as a member of the Advanced Radar Research Group. He is a member of the Technical Staff, Massachusetts Institute of Technology (MIT) Lincoln Laboratory. He holds one patent. He has authored or coauthored numerous papers in multiple journals and conferences and has also presented at these conferences. His expertise includes microwave circuit design, radar and communications systems design, and signal processing.

Mauricio Pinto (S'14) received the B.S. degree in electrical engineering from the California State Polytechnic University, Pomona, CA, USA, in 2010, the M.S. degree in engineering management from the University of Southern California, Los Angeles, CA, USA, in 2014, and is currently working toward the Ph.D. degree at the University of Colorado at Boulder, Boulder, CO, USA.

From 2010 to 2014, he was with the Weapons Division, Naval Air Warfare Center, CA, USA, where he was involved with RF front ends for various airborne and land-based defense systems.

Mike Coffey (S'10) received the B.S. degree in electrical engineering from the California State Polytechnic University, Pomona, CA, USA, in 2010, the M.S. degree in electrical engineering from the University of Colorado at Boulder, Boulder, CO, USA in 2014, and is currently working toward the Ph.D. degree at the University of Colorado at Boulder.

From 2010 to 2012, he was with the Advanced Technology Department, Wavestream Corporation, where he was involved with high-power X- and Ka-band satellite transmitters and transceivers for military and civilian applications. His current research interests include millimeter-wave (mmW) monolithic microwave integrated circuit (MMIC) power amplifier (PA) design, efficient and linear amplifier architectures, wireless power transfer, and nonlinear stability analysis techniques.

Mr. Coffey was the recipient of the College of Engineering Dean's Fellowship Award and the Electrical, Computer and Energy Engineering Merit Fellowship in 2012.

Zoya Popović (S'86–M'90–SM'99–F'02) received the Dipl.Ing. degree from the University of Belgrade, Serbia, Yugoslavia, in 1985, and the Ph.D. degree from the California Institute of Technology, Pasadena, CA, USA, in 1990.

Since 1990, she has been with the University of Colorado at Boulder, Boulder, CO, USA, where she is currently a Distinguished Professor and holds the Hudson Moore Jr. Chair with the Department of Electrical, Computer and Energy Engineering. She was named the 2015 University of Colorado Distinguished Lecturer. In 2001 and 2003, she was a Visiting Professor with the Technical University of Munich, Munich, Germany. In 2014, she was a Visiting Professor with ISAE, Toulouse, France. Since 1991, she has graduated 51 Ph.D. students. Her research interests include high-efficiency, low-noise, and broadband microwave and millimeter-wave circuits, active antennas, quasi-optical millimeter-wave techniques, applications of microwaves in medicine, intelligent RF front ends, and wireless powering for batteryless sensors.

Prof. Popović was the recipient of the 1993 and 2006 Microwave Prizes presented by the IEEE Microwave Theory and Techniques Society (IEEE MTT-S) for best journal papers. She received the 1996 URSI Issac Koga Gold Medal. She was named a National Science Foundation (NSF) White House Presidential Faculty Fellow in 1993. She was the recipient of a 2000 Humboldt Research Award for Senior U.S. Scientists from the German Alexander von Humboldt Stiftung. She was elected a Foreign Member of the Serbian Academy of Sciences and Arts in 2006. She was also the recipient of the 2001 Hewlett-Packard (HP)/American Society for Engineering Education (ASEE) Terman Medal for combined teaching and research excellence. She was the recipient of the IEEE MTT-S Distinguished Educator Award in 2013 and the 2015 Rudy Henning Distinguished Mentoring Award.